Nanoscale

ROYAL SOCIETY OF CHEMISTRY

PAPER

View Article Online
View Journal | View Issue

Check for updates

Cite this: *Nanoscale*, 2024, **16**, 5836

Optical grade transformation of monolayer transition metal dichalcogenides *via* encapsulation annealing†

Huije Ryu,‡[a] Seong Chul Hong,‡[a] Kangwon Kim,[b] Yeonjoon Jung,[a] Yangjin Lee,[c,d] Kihyun Lee,[c,d] Youngbum Kim,[e] Hyunjun Kim,[a] Kenji Watanabe,[f] Takashi Taniguchi,[g] Jeongyong Kim,[e] Kwanpyo Kim,[c,d] Hyeonsik Cheong[b] and Gwan-Hyoung Lee*[a]

Received 28th December 2023,
Accepted 26th February 2024

DOI: 10.1039/d3nr06641j

rsc.li/nanoscale

Monolayer transition metal dichalcogenides (TMDs) have emerged as highly promising candidates for optoelectronic applications due to their direct band gap and strong light–matter interactions. However, exfoliated TMDs have demonstrated optical characteristics that fall short of expectations, primarily because of significant defects and associated doping in the synthesized TMD crystals. Here, we report the improvement of optical properties in monolayer TMDs of MoS_2, $MoSe_2$, WS_2, and WSe_2, by hBN-encapsulation annealing. Monolayer WSe_2 showed 2000% enhanced photoluminescence quantum yield (PLQY) and 1000% increased lifetime after encapsulation annealing at 1000 °C, which are attributed to dominant radiative recombination of excitons through dedoping of monolayer TMDs. Furthermore, after encapsulation annealing, the transport characteristics of monolayer WS_2 changed from n-type to ambipolar, along with an enhanced hole transport, which also support dedoping of annealed TMDs. This work provides an innovative approach to elevate the optical grade of monolayer TMDs, enabling the fabrication of high-performance optoelectronic devices.

Introduction

Semiconducting TMDs have significant potential in optical applications owing to their large exciton binding energy, indirect-to-direct band transition, and strong light–matter interaction.[1–3] However, exfoliated or synthesized TMDs have shown different optical properties because they are strongly affected by several factors, such as doping, strain, chemical reaction, dielectric environment, and defects, that are also correlated.[4–12] For example, chalcogen vacancies cause n-type doping and provide non-radiative recombination pathways in the TMDs.[11] Numerous studies have demonstrated improvements in the PL of monolayer TMDs through various approaches, including decreasing chalcogen vacancies, electrostatically doping, or applying mechanical strain.[4,7,13,14] However, the critical factor responsible for the enhancement of PL remains elusive. This poses challenges in the fabrication of optical grade TMDs with optical properties approaching the theoretical upper limit. Here, we report a significant enhancement of optical properties in monolayer TMDs, including MoS_2, $MoSe_2$, WS_2, and WSe_2, by hBN-encapsulation annealing. Despite the 400% increase in defect density resulting from annealing hBN-encapsulated 1L-WSe_2 at 1000 °C, it astonishingly led to a remarkable 2000% increase in PL quantum yield (QY) and a 1000% extension in PL lifetime. Additionally, transport characteristics of the 1L-WS_2 transformed from n-type to ambipolar behavior along with an enhanced hole transport after encapsulation annealing. Our observation suggests that modulation of doping by hBN-encapsulation annealing plays a critical role in the optical grade of monolayer TMDs.

Results and discussion

For encapsulation annealing of monolayer TMDs, we fabricated stacks of hBN/TMDs/hBN using a pick-up technique.[15] Fig. 1a shows an optical microscopic image and atomic force

---

[a] *Department of Materials Science and Engineering, Seoul National University, Seoul 08826, Republic of Korea. E-mail: gwanlee@snu.ac.kr*
[b] *Department of Physics, Sogang University, Seoul 04107, Republic of Korea*
[c] *Department of Physics, Yonsei University, Seoul 03722, Republic of Korea*
[d] *Center for Nanomedicine, Institute for Basic Science, Seoul 03722, Republic of Korea*
[e] *Department of Energy Science, Sungkyunkwan University, Suwon 16419, Republic of Korea*
[f] *Research Center for Electronic and Optical Materials, National Institute for Materials Science, 1-1 Namiki, Tsukuba 305-0044, Japan*
[g] *Research Center for Materials Nanoarchitectonics, National Institute for Materials Science, 1-1 Namiki, Tsukuba 305-0044, Japan*

† Electronic supplementary information (ESI) available. See DOI: **https://doi.org/10.1039/d3nr06641j**

‡ These authors contributed equally to this work.

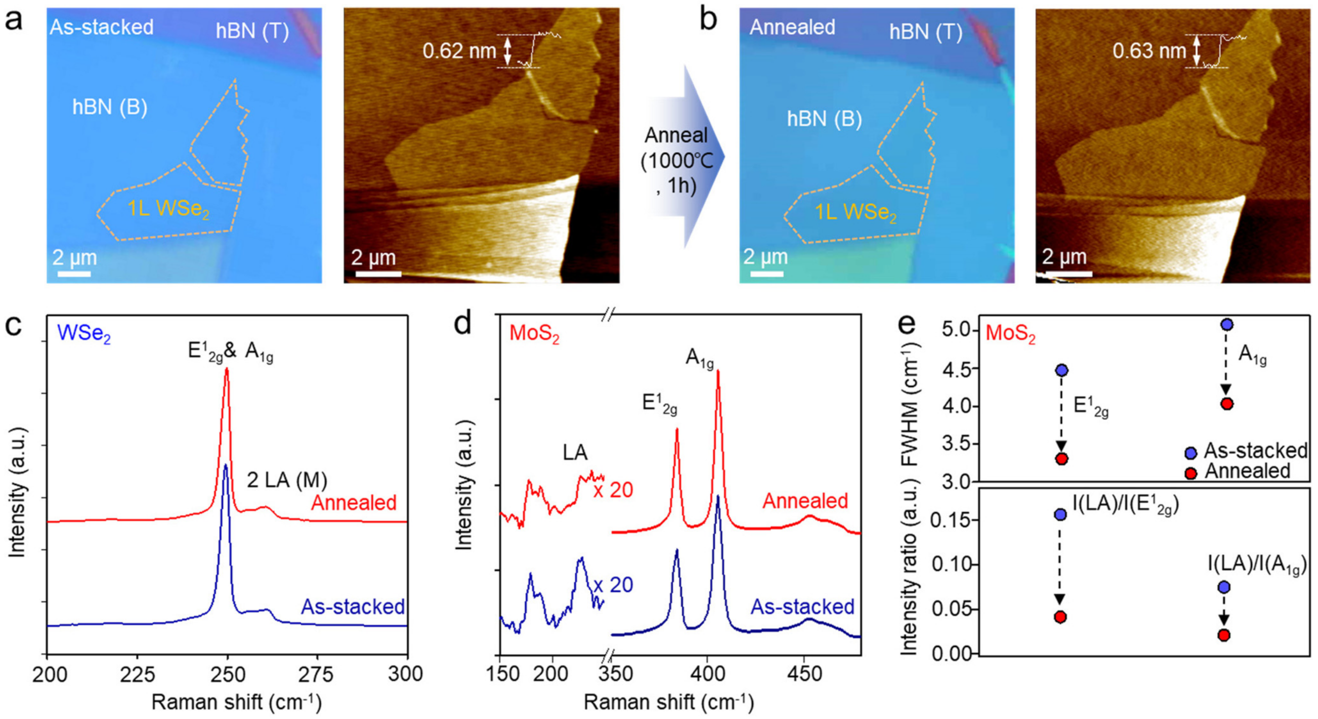

Fig. 1 hBN-encapsulation annealing of 1L-TMDs. Optical microscopic images (left) and AFM topography images (right) of hBN-encapsulated 1L-WSe_2 (a) before and (b) after annealing at 1000 °C. Raman spectra of hBN-encapsulated (c) 1L-WSe_2 and (d) 1L-MoS_2 before (blue) and after annealing (red). (e) FWHM of E^1_{2g} and A_{1g} peak (top) and intensity ratio of $I(LA)/I(E^1_{2g})$ and $I(LA)/I(A_{1g})$ (bottom) of hBN-encapsulated 1L-MoS_2 before (blue) and after annealing (red).

microscopy (AFM) topography image of the as-stacked hBN/1L-WSe_2/hBN. After being annealed at 1000 °C in vacuum for 1 hour, no significant change was observed as shown in Fig. 1b. Furthermore, as indicated by thickness profiles (white dashed lines) in Fig. 1a and b, there was no change in the thickness of the 1L-WSe_2 after encapsulation annealing. In contrast, the as-exfoliated 1L-WSe_2 on a SiO_2 substrate was thermally degraded and finally removed at 1000 °C during annealing (Fig. S1†), which is consistent with previous studies.[16,17] To examine the structural changes and doping effect due to encapsulation annealing, we measured the Raman spectra of hBN-encapsulated 1L-WSe_2 before and after annealing (Fig. 1c). After encapsulation annealing, no noticeable change was observed. To clearly identify the effect of strain and doping, we used 1L-MoS_2 as an indicator used in previous studies.[18–20] Fig. 1d shows the Raman spectra of hBN-encapsulated 1L-MoS_2 before and after annealing. The full width at half maximum (FWHM) of both A_{1g} and E^1_{2g} peaks decreased. Moreover, the encapsulation annealing process leads to a decrease in the intensity of the defect-related LA mode (~227 cm^{-1}) and an increase in the intensities of A_{1g} and E^1_{2g} peaks. These results are summarized in Fig. 1e: the FWHM values of A_{1g} and E^1_{2g} peaks and ratios of $I(LA)/I(A_{1g})$ and $I(LA)/I(E^1_{2g})$ decreased after encapsulation annealing. The position shifts of A_{1g} and E^1_{2g} peaks in Fig. S2 and S3† show that the 1L-MoS_2 becomes dedoped after encapsulation annealing.

To study the effect of encapsulation annealing on the optical properties of monolayer TMDs, we measured the PL spectra of 1L-WSe_2 before and after encapsulation annealing (Fig. 2a). After encapsulation annealing, the PL intensity of 1L-WSe_2 exhibited a significant increase by a factor of 8.8. The PL intensity map in Fig. 2b verifies that the PL was uniformly enhanced over whole area of 1L-WSe_2. To explore how annealing temperature influences the PL intensity, we assessed the PL intensity of the annealed hBN/1L-WSe_2/hBN and 1L-WSe_2/SiO_2 structures, as depicted in Fig. 2d. The annealing process was conducted in increments of 100 °C, spanning a range from T_{anneal} = 100 to 1000 °C. Up to 300 °C, the PL intensity for the hBN/1L-WSe_2/hBN remained almost unchanged. It was only after annealing at 400 °C that a noticeable increase in PL intensity became evident. Between 400 °C and 600 °C, there was a sharp increase in PL intensity, aligning with the temperature range where the trion/exciton intensity ratio and FWHM of A exciton peak rapidly decreases, as indicated in the inset of Fig. 2a and S4† respectively. Given that trions primarily follow a non-radiative pathway, the diminished trion/exciton ratio suggests that the radiative recombination of excitons dominates in our samples.[4] However, the PL intensity showed no further increase at higher temperature than 700 °C. In contrast, the 1L-WSe_2/SiO_2 showed a marked decline in PL intensity at 500 °C and no PL at higher temperature due to thermal degradation of WSe_2 (see Fig. S5† for PL spectra of 1L-WSe_2/SiO_2 before and after annealing at 1000 °C).

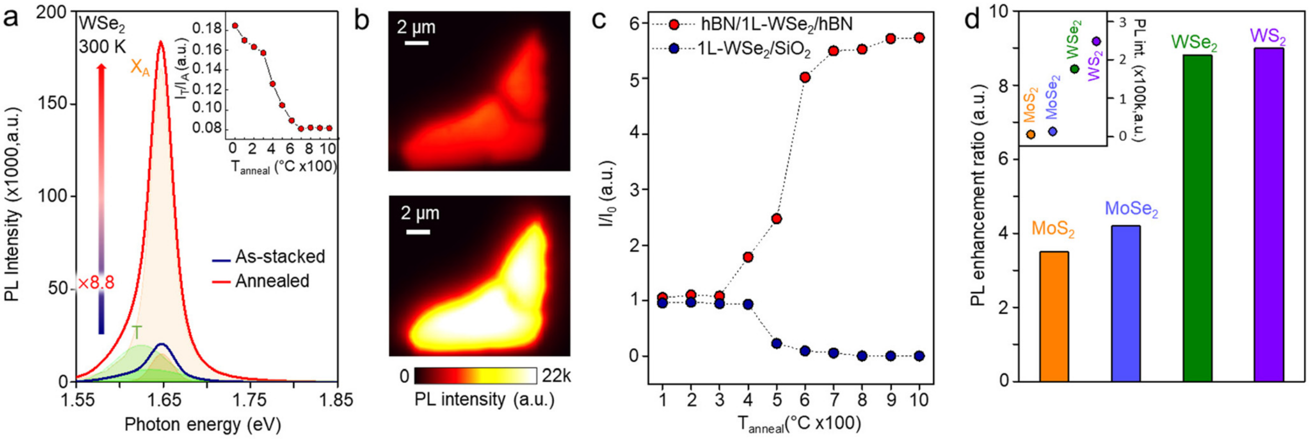

Fig. 2 PL enhancement of monolayer TMD by hBN-encapsulation annealing. (a) PL intensity spectra of hBN-encapsulated 1L-WSe$_2$ before (blue) and after annealing (red). Inset: Annealing temperature (100–1000 °C) dependent PL intensity ratio of trion and exciton. (b) PL intensity map of hBN-encapsulated 1L-WSe$_2$ before (top) and after annealing (bottom). (c) Annealing temperature dependent PL intensity of hBN/1L-WSe$_2$/hBN (red) and 1L-WSe$_2$/SiO$_2$ (blue) structures. (d) Bar plot indicating the PL enhancement factor for each 1L-MX$_2$ (M = Mo, W/X = S, Se) after encapsulation annealing. Inset: PL intensity of each monolayer TMD after encapsulation annealing.

Additionally, we annealed monolayers of MoS$_2$, MoSe$_2$, and WS$_2$ 1000 °C for 1 h, all encapsulated with hBN. As shown in Fig. 2d, it was verified that the enhancement in PL is not exclusive to WSe$_2$. The PL intensity of MoS$_2$, MoSe$_2$, and WS$_2$ increased by a factor of 3.5, 4.2, and 9, respectively. The PL intensities of these four monolayer TMDs after encapsulation annealing are displayed in the inset of Fig. 2d.

In Fig. 3, we investigated the optical properties of 1L-WSe$_2$ before and after encapsulation annealing. Fig. 3a and b show the PL contour plots of the as-stacked and annealed 1L-WSe$_2$ as a function of temperature, respectively. Below 100 K, there is no significant difference between PL intensity and peak positions of two samples. However, the A exciton (X_A) PL peak of annealed 1L-WSe$_2$ is higher than that of the as-stacked one

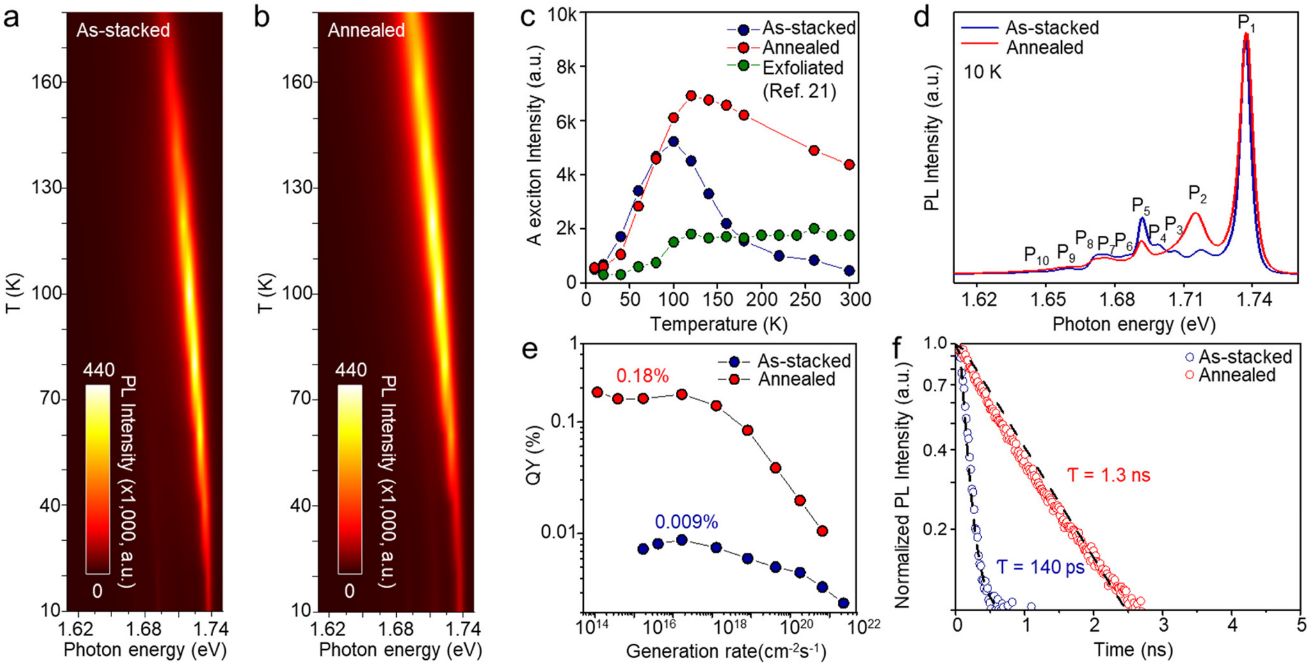

Fig. 3 Optical property measurement of hBN-encapsulated 1L-WSe$_2$ before and after annealing. Contour plots of PL spectra of hBN-encapsulated 1L-WSe$_2$ as a function of temperature (10–180 K) (a) before and (b) after annealing. (c) A exciton intensity as a function of temperature of exfoliated 1L-WSe$_2$ (green), hBN-encapsulated 1L-WSe$_2$ before (blue) and after annealing (red). (d) PL spectra (10 K) of hBN-encapsulated 1L-WSe$_2$ before (blue) and after annealing (red). (e) Plot of QY as a function of the generation rate and (f) normalized TRPL decay curves for hBN-encapsulated 1L-WSe$_2$ before (blue) and after annealing (red).

above 100 K. Fig. 3c shows the temperature-dependent A exciton PL intensities of the two samples. As the temperature decreases, the PL intensity of both samples increases, then decreases around 100 and 120 K for as-stacked and annealed 1L-WSe_2, respectively. This is in contrast to the previous report that the PL intensity continuously is reduced as the temperature decreases due to the dominant population of dark excitons of WSe_2, which is shown in Fig. 3c.[21] The high quality WSe_2 synthesized by a flux method in ref. 21 shows the similar trend in the temperature-dependent measurement of PL because of the interplay between defect- and phonon-scattering and the dark exciton state. It is noteworthy that, even though hBN-encapsulation enhances the PL of WSe_2, additionally annealed WSe_2 shows higher PL intensity in the temperature range above 100 K. Fig. 3d shows the PL spectra of as-stacked and annealed 1L-WSe_2 measured at 10 K. The individual PL peaks correspond to the A exciton (P_1), biexciton (P_2), intervalley trion (P_3), intravalley trion (P_4), negatively charged biexciton (P_5), and localized excitons (P_6–P_{10}), respectively as indicated in Fig. 3d.[22–24] At 10 K, spin-forbidden dark excitons are prevalent and A exciton PL peaks of both samples show no significant difference. However, after encapsulation annealing, the negatively charged biexciton (P_5) is suppressed, while the biexciton (P_2) is enhanced. This phenomenon can also be attributed to a dedoping effect as a higher concentration of biexcitons is expected in neutralized WSe_2 compared to negatively charged biexcitons. In the case of hBN-encapsulation annealed 1L-MoS_2 with bright excitons (Fig. S6†),[25] the PL intensity increases with decreasing temperature and A exciton PL peak becomes much higher after encapsulation annealing due to the dedoping effect.

Next, we measured the PL QY of as-stacked and annealed 1L-WSe_2 in Fig. 3e. The annealed 1L-WSe_2 exhibited higher PL QY of 0.18% at a generation rate of 10^{17} cm^{-2} s^{-1} by 20 times than that of the as-stacked 1L-WSe_2 (0.009%). The significant improvement in PL QY can be ascribed to the prevalent formation of neutral excitons, which predominantly follow a radiative recombination path. We also verified that the PL QY of annealed 1L-MoS_2 increases by a factor of 5 (Fig. S7a†). To analyze the exciton recombination dynamics of annealed WSe_2, time-resolved photoluminescence (TRPL) measurements were performed in Fig. 3f. The PL decay curves were fitted with a single exponential decay function, $I(t) = \int_{-\infty}^{t} \mathrm{IRF}(t')\mathrm{e}^{-\frac{t-t'}{\tau}}\mathrm{d}t$, where IRF is a Gaussian instrument response function.[26] The annealed WSe_2 exhibits a relatively prolonged lifetime of 1.3 ns, surpassing that of the as-stacked one by an order of magni-

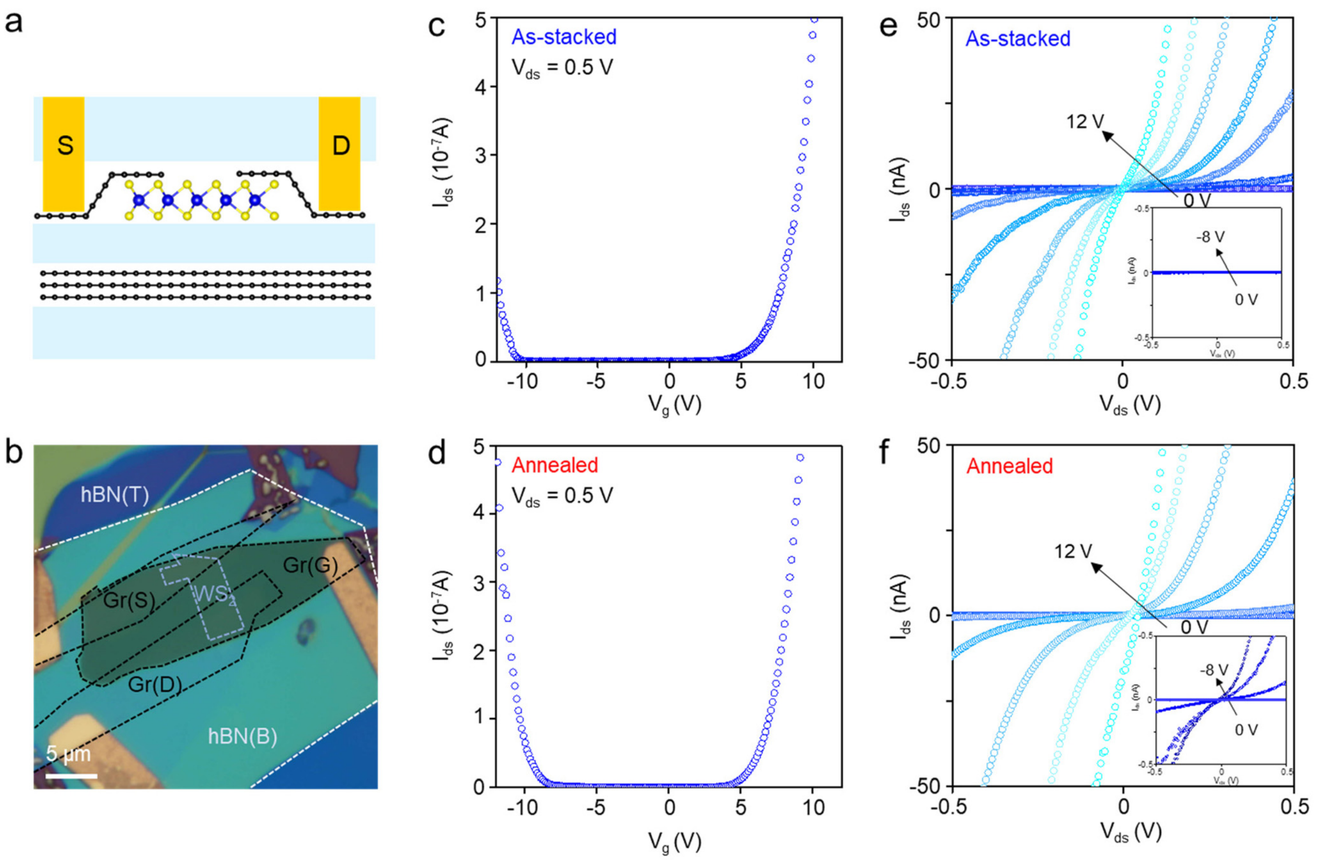

Fig. 4 Electrical properties of hBN/1L-WS_2/hBN (WS_2 FET) device before and after annealing. (a) Schematic illustration and (b) optical microscopic image of the fabricated WS_2 device. I_{ds}–V_g characteristics for WS_2 FET (c) before and (d) after annealing. I_{ds}–V_{ds} characteristics for WS_2 FET (e) before and (f) after annealing as a function of gate voltage (V_g) ranging from 0 to 12 V for n-type transport and 0 to −8 V for p-type transport (inset).

tude. The recombination lifetime (τ_{ob}) is determined by combination of the radiative (τ_r) and nonradiative (τ_{nr}) lifetimes as per the following equation:

$$\frac{1}{\tau_{ob}} = \frac{1}{\tau_r} + \frac{1}{\tau_{nr}}.$$

Because the radiative lifetime is longer than nonradiative lifetime by an order of magnitude, the prolonged lifetime of the annealed WSe_2 indicates that the radiative recombination of neutral excitons is dominant and the formation of trions with nonradiative recombination is suppressed due to the dedoping effect.[26,27] The annealed 1L-MoS_2 also showed an increased lifetime as shown in Fig. S7b.†

The effects of encapsulation annealing on the electrical properties of monolayer TMDs are investigated in Fig. 4. We fabricated an hBN-encapsulated 1L-WS_2 device with graphene electrodes as shown in the schematic of Fig. 4a. Fig. 4b shows an optical microscopic image of a representative 1L-WS_2 device. As shown in transport curves of Fig. 4c and d, the 1L-WS_2 device exhibited enhanced p-type transport after encapsulation annealing. This result also supports that the WS_2 channel is dedoped as confirmed by the Raman spectroscopic measurements and PL analyses in Fig. S3† and Fig. 3. Despite dedoping induced by encapsulation annealing, the field effect mobility for electrons increased from 4.94 to 5.14 $cm^2\ V^{-1}\ s^{-1}$. The n-type transport properties of the 1L-WS_2 remained consistent, whereas the p-type transport exhibited enhancement after encapsulation annealing, as shown in the output curves of Fig. 4e and f. These findings indicate that the dedoping induced by encapsulation annealing results in alterations in the electrical properties, while still preserving high electrical performance.

To probe the structural changes of 1L-WSe_2 during encapsulation annealing, we employed scanning transmission electron microscopy (STEM) in Fig. 5a–c. For the STEM characterization, 1L-graphene was used as an encapsulation layer as the graphene has a small background signal (see Methods for details of the TEM sample preparation).[28–30] The high-angle annular dark field (HAADF) STEM images of Fig. 5a and b show the atomic structures of as-stacked and annealed 1L-WSe_2. We calculated the defect densities of two samples using a deep learning process with 1000 simulated STEM images (1024 × 1024 pixels) as we previously reported.[31] The defect density increased from 0.33% to 1.38% (see the ESI† for details of the defect density calculation). This is contrary to previous reports that defect density and PL intensity have an inverse correlation.[32] In order to differentiate the types of defects in as-stacked and annealed WSe_2, we plot the defect

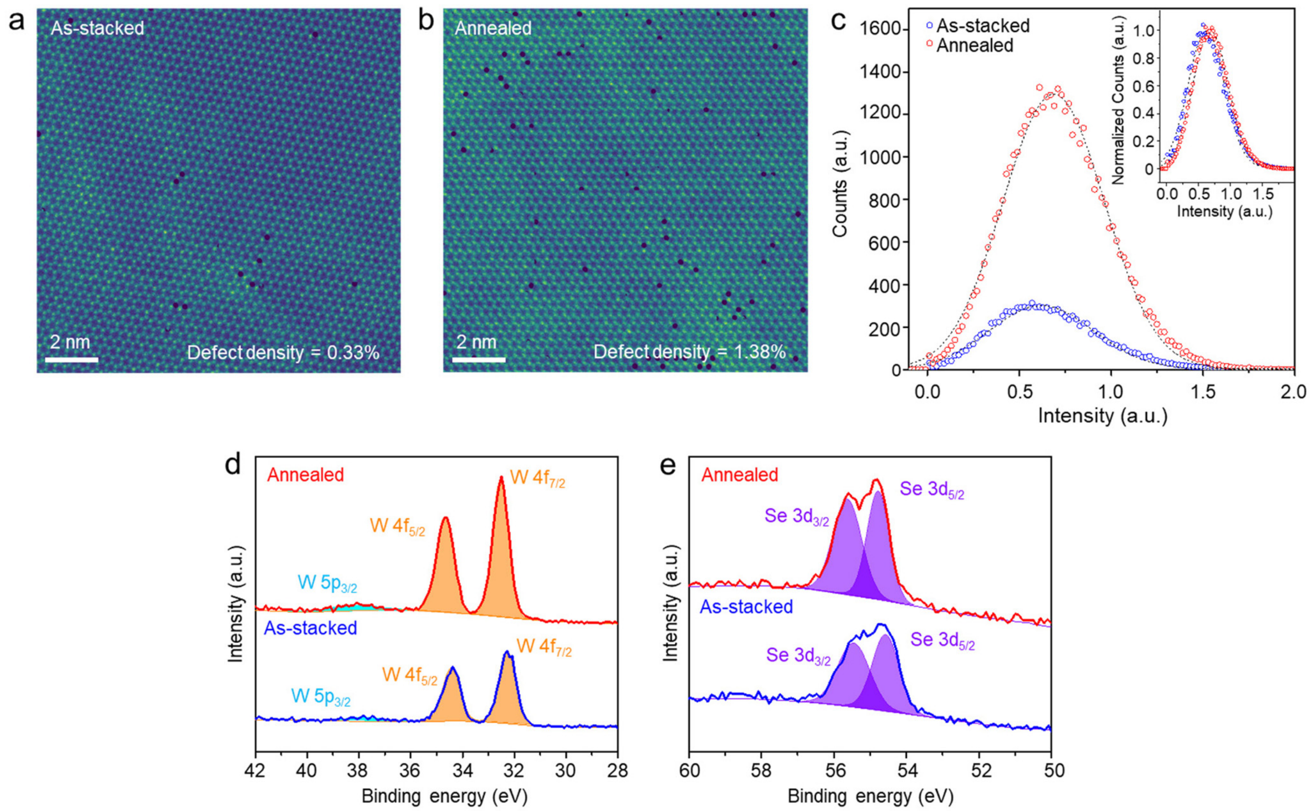

Fig. 5 Structural analysis of hBN-encapsulated WSe_2 before and after annealing. HAADF-STEM image of graphene-encapsulated 1L-WSe_2 (a) before and (b) after annealing. (c) Spectra of number of defects per total atoms as a function of intensity of defect sites in 1L-WSe_2 before (blue) and after annealing (red). Inset: Normalized Spectra. XPS spectra of (d) W 4f, (e) Se 3d core levels of hBN-encapsulated 2L-WSe_2 before and after annealing.

density, *i.e.* counts, as a function of contrast intensity of STEM images as shown in Fig. 5c. It is clear that the encapsulation annealed WSe_2 has more defects with relatively high contrast intensity as shown in the inset of Fig. 5c. The vacant sites in defects with higher contrast intensity might be substituted by impurities, such as oxygen, because it has been reported that chalcogen vacancies are substituted by oxygen during post treatments, such as thermal annealing and laser exposure, leading to reduction of vacancy-induced in-gap states below the conduction band.[27,33–40]

To examine the compositions of as-stacked and annealed WSe_2, X-ray photoelectron spectroscopy (XPS) was used. Note that we used 2L-WSe_2 for XPS measurements as the monolayer generates low signals. Fig. 5d and e show the XPS spectra of W 4f and Se 3d core levels before and after encapsulation annealing, respectively. The three distinct features of the W $4f_{7/2}$, W $4f_{5/2}$, and W $5p_{3/2}$ are observed at 32.3, 34.4, and 37.6 eV, respectively. The doublets observed at 54.6 and 55.5 eV correspond to the Se $3d_{5/2}$ and Se $3d_{3/2}$.[41] After encapsulation annealing, the binding energies of W 4f and Se 3d core-levels blueshifted, possibly indicating improved crystallinity. Based on our observed results, the origin of the dedoping effect induced by encapsulation annealing can be ascribed to the substitution of vacancies with oxygen and the enhanced crystallinity in defect-free areas.

Conclusions

In conclusion, we demonstrate a hBN-encapsulation annealing method to achieve the optical grade of monolayer TMDs. After annealing at 1000 °C for 1 h, we observed enhancement of PL intensity, QY, and lifetime in hBN-encapsulated 1L-TMD. The hBN-encapsulated 1L-WS_2 exhibited a transition in the transport characteristics from n-type to ambipolar behavior, which can be attributed to the dedoping of WS_2 after encapsulation annealing. STEM measurements indicated an increase of defect density after encapsulation annealing. Our observation that the n-type TMD undergoes dedoping despite increased defect density is an exceptional case. Our deep learning analysis implies that the majority of the newly introduced defects might be impurities rather than selenium vacancies. Our work shows a novel way to transform monolayer TMDs into optical grade materials by the hBN-encapsulation annealing and has great potential for various optoelectronic applications.

Methods

Chemical vapor deposition growth

1L-MoS_2 crystals were grown on silicon dioxide/silicon (SiO_2/Si) substrates with SiO_2 thickness of 285 nm by the CVD method within a 2-inch quartz tube, conducted under atmospheric pressure. To synthesize 1L-MoS_2, a quartz boat containing MoO_3 powder (99.97%, Sigma-Aldrich) was positioned in the center of a furnace, and a SiO_2/Si substrate was suspended face-down on top of the boat. Another quartz boat loaded with sulfur powder (Sigma-Aldrich) was located upstream within the quartz tube, approximately 21.5 centimeters away from the center of the furnace. The furnace temperature was gradually increased to 750 °C at a rate of 50 °C per minute and maintained for 15 minutes, and then the furnace was naturally cooled to room temperature. Ar (300 sccm) was flowed for the entire growth process.

Sample preparation

2D flakes utilized in the fabrication process were mechanically exfoliated onto SiO_2/Si substrates. The thickness of each material was individually verified using a combination of Atomic Force Microscopy (AFM) and optical contrast. To encapsulate monolayer TMD between hBN, the pick-up transfer technique was used with a polypropylene carbonate (bisphenol A carbonate, Sigma Aldrich) (PC)-coated poly (dimethyl siloxane) (PDMS) lens mounted on a slide glass to pick-up and release.[15] The PDMS/PC/slide glass assembly was manipulated using a 3-axis micromanipulator to control the position of the contact area. By solely regulating the stage temperature within the range of 80–130 °C, the top hBN was picked up completely by the PC, ensuring there were no cracks or folds. Once the hBN had been separated from the substrates, monolayer TMD and the bottom hBN were picked-up by van der Waals forces from the top hBN to form hBN/1L-TMD/hBN ultrathin 2D heterostructures. It's important to note that monolayer TMD had to be fully encapsulated by hBN without any bubbles; otherwise, the monolayer TMD would degrade during the annealing process. After stacking, the heterostructure was transferred onto a clean SiO_2/Si substrate by releasing the PC film from the PDMS lens at a temperature exceeding 180 °C. Finally, to remove the PC film, the samples were immersed in chloroform for 30 minutes. Similar to hBN-encapsulated monolayer TMDs, graphene-encapsulated monolayer TMDs for STEM imaging were also prepared using the dry-transfer method.[29,30] To prevent degradation of heterostructures during annealing, bi- or trilayer graphene was used. Nonetheless, removing graphene from the SiO_2/Si substrate proves challenging due to the stronger adhesion of Gr/SiO_x in comparison to hBN/SiO_x.[42] Therefore, hBN was employed as the upper layer to facilitate the easy detachment of the graphene. Thus, hBN/Gr/TMDs/Gr heterostructures were fabricated initially. Next, XeF_2 gas, which can selectively etch only hBN remaining on the graphene, was treated on the heterostructures to remove the top hBN.[28] For the encapsulation annealing of monolayer TMD, the sandwiched 1L-TMD was annealed in a vacuum of 10^{-4} Torr. The furnace temperature was ramped up to the target annealing temperature for 3 h and maintained for 1 h. Then, the furnace was naturally cooled to room temperature.

Raman and PL spectroscopy

Room-temperature Raman and PL intensity map images and spectra were obtained using a Raman spectroscopy instrument equipped with a 532 nm laser and a spot size of ~1 μm

(JASCO). To minimize any potential damage to the sample caused by laser exposure, a power of <5 mW was used for an acquisition time of 60 s. Given that the laser spot size was approximately 1 μm, the mapping area was scanned with a point-to-point distance of 1 μm. Low-temperature micro-photoluminescence (micro-PL) measurements were carried out using a diode-pumped solid-state laser with wavelength of 532 nm (2.33 eV) and power of ~5 μW. We used a 40× objective lens (numerical aperture 0.6) to focus the laser on the samples with a spot of diameter ~1 μm and to collect PL signals from samples. A substrate with hBN-encapsulated 1L-TMD samples was loaded into an optical cryostat (Oxford MicrostatHe2) and cooled to 10 K with liquid helium. PL signals emitted by the samples were spectrally resolved using a Horiba TRIAX 320 spectrometer (300 grooves per mm) and were detected with a thermoelectrically cooled charge-coupled device (CCD) camera. Raman and PL spectra were obtained at the same position before and after annealing.

Atomic force microscopy

AFM (Park Systems, NX10) in the contact mode was used to observe the surface morphology, and thickness of hBN-encapsulated 1L-WSe_2.

Quantum yield measurement

To estimate the QY of 1L-WSe_2 and MoS_2, we encapsulated a mechanically exfoliated 1L-WSe_2 flake and CVD-grown 1L-MoS_2 with hBN and transferred it onto a SiO_2 substrate. As a reference sample, we utilized a thin poly(methyl methacrylate) (PMMA) film that contained dispersed rhodamine 6G (R6G).[43–45] We acquired photoluminescence (PL) spectra from a 300 nm-thick PMMA film with a concentration of 10^{-4} M of R6G and from a bare quartz substrate. These spectra were measured utilizing an integrating sphere under a 514 nm laser excitation. We estimated the QY of the reference sample from the emission and absorption of the R6G. Next, we conducted photoluminescence (PL) intensity and absorption measurements on the hBN-encapsulated 1L-WSe_2 and MoS_2 using a confocal microscope under identical measurement conditions. By comparing the PL intensity and absorption of 1L-WSe_2 and MoS_2 with those of the reference sample, we were able to estimate the quantum yield (QY) of 1L-WSe_2 and MoS_2.

Time resolved-PL measurement

For TRPL measurements, we employed the same microscope, which was equipped with a pulsed excitation at 488 nm (BDL-488, Becker & Hickl GmbH), with a pulse width of 70 ps and a repetition rate of 80 MHz, along with a high-speed hybrid detector (HPM-100-40, Becker & Hickl GmbH) and a time-correlated single-photon counting module (TCSPC, Becker & Hickl GmbH). All measurements were conducted at room temperature.

Device fabrication and electrical measurement

Electron beam lithography was utilized to develop metal pad patterns and establish *via* contacts for graphene electrodes encapsulated by hBN. The van der Waals heterostructure was etched by exposing the pre-patterned structure to XeF_2.[28] The top hBN was etched away, and the embedded graphene electrodes stopped the etching process. Metals of Cr/Pd/Au (1 nm/30 nm/40 nm) were then deposited on the exposed graphene electrodes using an e-beam evaporator. Subsequently, a lift-off process was carried out by immersing the samples in acetone. Electrical measurements of the devices were then conducted at room temperature under ambient conditions, employing a parameter analyzer, specifically the Keithley 2400.

Transmission electron microscopy

Transmission electron microscopy samples were prepared using a poly(methyl methacrylate)-based wet-transfer method. Samples on poly(methyl methacrylate) film were transferred on Si_3N_4 nanofilm TEM grids (TEM Windows, SN100-A10Q33B). The PMMA film was removed by placing samples in acetone for 12 h. A double-Cs-aberration-corrected JEOL ARM-200F was used for HAADF-STEM images at an operating voltage of 80 kV with a 23 mrad convergence angle and collection semi angles from 68 to 280 mrad.

Model building and training

We generated a ResUNet deep learning model with 5 residual blocks and gradual increased filters from 32 to 128 in the convolutional layers to evaluate the number and type of defects in WSe_2. We used 1000 simulated STEM images (1024 × 1024 pixels) of WSe_2 as training and validation data. The loss function (categorical cross entropy) decreased under 0.03.[31] Pixels with defects were extracted by the model, and we averaged the pixel's intensity out to compare annealed and as-stacked sample. We confirmed that the local intensity of the annealed Se vacancies was higher than that of untreated Se vacancies, which may represent oxygen adsorbed on Se vacancy sites during annealing.

X-ray photoelectron spectroscopy

XPS samples were prepared with a top hBN layer approximately 3 nm thick to ensure a distinct signal. The XPS spectra of W and Se are obtained with Al Kα radiation using a 10 μm beam spot size (Versaprobe III).

Author contributions

H. R. and G.-H. L. designed and conceived the project. K. W. K. and H. C. performed PL measurements at low temperature. Y. J. synthesized TMDs by CVD. Y. L. and K. P. K. performed HAADF-STEM imaging. K. L. and K. P. K. performed STEM image analysis based on deep learning. Y. K. and J. K. performed QY and TRPL measurements. H. K. performed XPS measurements. K. W. and T. T. supplied boron nitride crystals. H. R., S. C. H., and G.-H. L. collectively analyzed the data and wrote the paper. All authors read and contributed to the manuscript.

Conflicts of interest

There are no conflicts to declare.

Acknowledgements

This research was supported by the National Research Foundation of Korea (NRF) funded by the Ministry of Science and ICT (NRF-2021R1A2C301431613, NRF-2019R1A2C3006189, and NRF-2017R1A5A1014862 (SRC program: vdWMRC center)) and the Creative-Pioneering Researchers Program through Seoul National University (SNU). K. W. and T. T. acknowledge support from the JSPS KAKENHI (Grant Numbers 21H05233 and 23H02052) and World Premier International Research Center Initiative (WPI), MEXT, Japan. G.-H. L. acknowledges the support from the Research Institute of Advanced Materials (RIAM), Institute of Engineering Research (IER), Institute of Applied Physics (IAP), and Inter-University Semiconductor Research Center (ISRC) at the Seoul National University.

References

1 A. Raja, A. Chaves, J. Yu, G. Arefe, H. M. Hill, A. F. Rigosi, T. C. Berkelbach, P. Nagler, C. Schuller, T. Korn, C. Nuckolls, J. Hone, L. E. Brus, T. F. Heinz, D. R. Reichman and A. Chernikov, *Nat. Commun.*, 2017, **8**, 15251.
2 Q. H. Wang, K. Kalantar-Zadeh, A. Kis, J. N. Coleman and M. S. Strano, *Nat. Nanotechnol.*, 2012, **7**, 699–712.
3 X. Liu, T. Galfsky, Z. Sun, F. Xia, E.-c. Lin, Y.-H. Lee, S. Kéna-Cohen and V. M. Menon, *Nat. Photonics*, 2015, **9**, 30–34.
4 D.-H. Lien, S. Z. Uddin, M. Yeh, M. Amani, H. Kim, J. W. Ager, E. Yablonovitch and A. Javey, *Science*, 2019, **364**, 468–471.
5 E. Ji, K. Yang, J. C. Shin, Y. Kim, J. W. Park, J. Kim and G.-H. Lee, *Nanoscale*, 2022, **14**, 14106–14112.
6 S. Kang, Y. S. Kim, J. H. Jeong, J. Kwon, J. H. Kim, Y. Jung, J. C. Kim, B. Kim, S. H. Bae, P. Y. Huang, J. C. Hone, H. Y. Jeong, J. W. Park, C. H. Lee and G.-H. Lee, *ACS Appl. Mater. Interfaces*, 2021, **13**, 1245–1252.
7 H. Kim, S. Z. Uddin, N. Higashitarumizu, E. Rabani and A. Javey, *Science*, 2021, **373**, 448–452.
8 M. Amani, D.-H. Lien, D. Kiriya, J. Xiao, A. Azcatl, J. Noh, S. R. Madhvapathy, R. Addou, S. Kc, M. Dubey, K. Cho, R. M. Wallace, S.-C. Lee, J.-H. He, J. W. Ager, X. Zhang, E. Yablonovitch and A. Javey, *Science*, 2015, **350**, 1065–1068.
9 F. Cadiz, E. Courtade, C. Robert, G. Wang, Y. Shen, H. Cai, T. Taniguchi, K. Watanabe, H. Carrere, D. Lagarde, M. Manca, T. Amand, P. Renucci, S. Tongay, X. Marie and B. Urbaszek, *Phys. Rev. X*, 2017, **7**, 021026.
10 Y. Lin, X. Ling, L. Yu, S. Huang, A. L. Hsu, Y.-H. Lee, J. Kong, M. S. Dresselhaus and T. Palacios, *Nano Lett.*, 2014, **14**, 5569–5576.
11 L. Li and E. A. Carter, *J. Am. Chem. Soc.*, 2019, **141**, 10451–10461.
12 H. Y. Jeong, Y. Jin, S. J. Yun, J. Zhao, J. Baik, D. H. Keum, H. S. Lee and Y. H. Lee, *Adv. Mater.*, 2017, **29**, 1605043.
13 X. Zhang, Q. Liao, S. Liu, Z. Kang, Z. Zhang, J. Du, F. Li, S. Zhang, J. Xiao, B. Liu, Y. Ou, X. Liu, L. Gu and Y. Zhang, *Nat. Commun.*, 2017, **8**, 15881.
14 A. O. A. Tanoh, J. Alexander-Webber, Y. Fan, N. Gauriot, J. Xiao, R. Pandya, Z. Li, S. Hofmann and A. Rao, *Nanoscale Adv.*, 2021, **3**, 4216–4225.
15 L. Wang, I. Meric, P. Y. Huang, Q. Gao, Y. Gao, H. Tran, T. Taniguchi, K. Watanabe, L. M. Campos, D. A. Muller, J. Guo, P. Kim, J. Hone, K. L. Shepard and C. R. Dean, *Science*, 2013, **342**, 614–617.
16 W. H. Blades, N. J. Frady, P. M. Litwin, S. J. McDonnell and P. Reinke, *J. Phys. Chem. C*, 2020, **124**, 15337–15346.
17 P. Chen, W. Xu, Y. Gao, P. Holdway, J. H. Warner and M. R. Castell, *J. Phys. Chem. C*, 2019, **123**, 3876–3885.
18 R. Rao, A. E. Islam, S. Singh, R. Berry, R. K. Kawakami, B. Maruyama and J. Katoch, *Phys. Rev. B*, 2019, **99**, 195401.
19 M. Velicky, A. Rodriguez, M. Bousa, A. V. Krayev, M. Vondracek, J. Honolka, M. Ahmadi, G. E. Donnelly, F. Huang, H. D. Abruna, K. S. Novoselov and O. Frank, *J. Phys. Chem. Lett.*, 2020, **11**, 6112–6118.
20 S. Mignuzzi, A. J. Pollard, N. Bonini, B. Brennan, I. S. Gilmore, M. A. Pimenta, D. Richards and D. Roy, *Phys. Rev. B: Condens. Matter Mater. Phys.*, 2015, **91**, 195411.
21 D. Edelberg, D. Rhodes, A. Kerelsky, B. Kim, J. Wang, A. Zangiabadi, C. Kim, A. Abhinandan, J. Ardelean, M. Scully, D. Scullion, L. Embon, R. Zu, E. J. G. Santos, L. Balicas, C. Marianetti, K. Barmak, X. Zhu, J. Hone and A. N. Pasupathy, *Nano Lett.*, 2019, **19**, 4371–4379.
22 M. Barbone, A. R. Montblanch, D. M. Kara, C. Palacios-Berraquero, A. R. Cadore, D. De Fazio, B. Pingault, E. Mostaani, H. Li, B. Chen, K. Watanabe, T. Taniguchi, S. Tongay, G. Wang, A. C. Ferrari and M. Atature, *Nat. Commun.*, 2018, **9**, 3721.
23 T. P. Lyons, S. Dufferwiel, M. Brooks, F. Withers, T. Taniguchi, K. Watanabe, K. S. Novoselov, G. Burkard and A. I. Tartakovskii, *Nat. Commun.*, 2019, **10**, 2330.
24 J. Jadczak, J. Kutrowska-Girzycka, P. Kapuscinski, Y. S. Huang, A. Wojs and L. Bryja, *Nanotechnology*, 2017, **28**, 395702.
25 M. Koperski, M. R. Molas, A. Arora, K. Nogajewski, A. O. Slobodeniuk, C. Faugeras and M. Potemski, *Nanophotonics*, 2017, **6**, 1289–1308.
26 L. Yuan and L. Huang, *Nanoscale*, 2015, **7**, 7402–7408.
27 Z. Luo, W. Zheng, N. Luo, B. Liu, B. Zheng, X. Yang, D. Liang, J. Qu, H. Liu, Y. Chen, Y. Jiang, S. Chen, X. Zou and A. Pan, *Nano Lett.*, 2022, **22**, 2112–2119.
28 J. Son, J. Kwon, S. Kim, Y. Lv, J. Yu, J. Y. Lee, H. Ryu, K. Watanabe, T. Taniguchi, R. Garrido-Menacho, N. Mason, E. Ertekin, P. Y. Huang, G.-H. Lee and A. M. van der Zande, *Nat. Commun.*, 2018, **9**, 3988.
29 H. Ryu, Y. Lee, H. J. Kim, S. H. Kang, Y. Kang, K. Kim, J. Kim, B. E. Janicek, K. Watanabe, T. Taniguchi,

P. Y. Huang, H. Cheong, I. H. Jung, K. Kim, Y. W. Son and G.-H. Lee, *Adv. Funct. Mater.*, 2021, **31**, 2107376.

30 H. Ryu, Y. Lee, J. H. Jeong, Y. Lee, Y. Cheon, K. Watanabe, T. Taniguchi, K. Kim, H. Cheong, C. H. Lee and G.-H. Lee, *Small*, 2023, **19**, 2205224.

31 K. Lee, J. Park, S. Choi, Y. Lee, S. Lee, J. Jung, J. Y. Lee, F. Ullah, Z. Tahir, Y. S. Kim, G. H. Lee and K. Kim, *Nano Lett.*, 2022, **22**, 4677–4685.

32 M. R. Rosenberger, H.-J. Chuang, K. M. McCreary, C. H. Li and B. T. Jonker, *ACS Nano*, 2018, **12**, 1793–1800.

33 X. Wei, Z. Yu, F. Hu, Y. Cheng, L. Yu, X. Wang, M. Xiao, J. Wang, X. Wang and Y. Shi, *AIP Adv.*, 2014, **4**, 123004.

34 C. Hou, J. Deng, J. Guan, Q. Yang, Z. Yu, Y. Lu, Z. Xu, Z. Yao and J. Zheng, *Phys. Chem. Chem. Phys.*, 2021, **23**, 24579–24588.

35 H. Ardekani, R. Younts, Y. Yu, L. Cao and K. Gundogdu, *ACS Appl. Mater. Interfaces*, 2019, **11**, 38240–38246.

36 S. V. Sivaram, A. T. Hanbicki, M. R. Rosenberger, G. G. Jernigan, H. J. Chuang, K. M. McCreary and B. T. Jonker, *ACS Appl. Mater. Interfaces*, 2019, **11**, 16147–16155.

37 H. Nan, Z. Wang, W. Wang, Z. Liang, Y. Lu, Q. Chen, D. He, P. Tan, F. Miao, X. Wang, J. Wang and Z. Ni, *ACS Nano*, 2014, **8**, 5738–5745.

38 P.-C. Shen, Y. Lin, C. Su, C. McGahan, A.-Y. Lu, X. Ji, X. Wang, H. Wang, N. Mao, Y. Guo, J.-H. Park, Y. Wang, W. Tisdale, J. Li, X. Ling, K. E. Aidala, T. Palacios and J. Kong, *Nat. Electron.*, 2022, **5**, 28–36.

39 C. Schwermann, T. Stiehm, P. Tonndorf, R. Schneider, R. Schmidt, J. Kern, S. Michaelis de Vasconcellos, R. Bratschitsch and N. L. Doltsinis, *Phys. Chem. Chem. Phys.*, 2018, **20**, 16918–16923.

40 Z. Hu, J. Avila, X. Wang, J. F. Leong, Q. Zhang, Y. Liu, M. C. Asensio, J. Lu, A. Carvalho, C. H. Sow and A. H. Castro Neto, *Nano Lett.*, 2019, **19**, 4641–4650.

41 F. Bozheyev, K. Harbauer, C. Zahn, D. Friedrich and K. Ellmer, *Sci. Rep.*, 2017, **7**, 16003.

42 H. Rokni and W. Lu, *Nat. Commun.*, 2020, **11**, 5607.

43 S. Roy, A. S. Sharbirin, Y. Lee, W. B. Kim, T. S. Kim, K. Cho, K. Kang, H. S. Jung and J. Kim, *Nanomaterials*, 2020, **10**, 1032.

44 D. Pan, Y. Fu, N. Spitha, Y. Zhao, C. R. Roy, D. J. Morrow, D. D. Kohler, J. C. Wright and S. Jin, *Nat. Nanotechnol.*, 2021, **16**, 159–165.

45 K. Chen, S. Deng, E. Chen, S. Wen, T. Ouyang, X. Wang, R. Zhan, J. Cai, X. Wan and H. Chen, *ACS Appl. Mater. Interfaces*, 2021, **13**, 44814–44823.